

# The Cosmic Infrared Background seen by ALMA

S. Carniani<sup>1,2,3</sup>, R. Maiolino<sup>2,3</sup>, G. De Zotti<sup>4,5</sup>, M. Negrello<sup>5</sup>, A. Marconi<sup>1</sup>, M. Botwhell<sup>2</sup>, P. Capak<sup>6,7</sup>, C. Carilli<sup>2,8</sup>,  
M. Castellano<sup>9</sup>, S. Cristiani<sup>10</sup>, A. Ferrara<sup>11</sup>, A. Fontana<sup>9</sup>, S. Gallerani<sup>11</sup>, G. Jones<sup>12</sup>, K. Ohta<sup>13</sup>, K. Ota<sup>2,3</sup>, L.  
Pentericci<sup>9</sup>, P. Santini<sup>9</sup>, K. Sheth<sup>6,7</sup>, L. Vallini<sup>14</sup>, E. Vanzella<sup>15</sup>, J. Wagg<sup>2,3,16</sup>, R. J. Williams<sup>2,3</sup>

<sup>1</sup> Dipartimento di Fisica e Astronomia, Università di Firenze, Via G. Sansone 1, I-50019, Sesto Fiorentino (Firenze), Italy

<sup>2</sup> Cavendish Laboratory, University of Cambridge, 19 J. J. Thomson Ave., Cambridge CB3 0HE, UK

<sup>3</sup> Kavli Institute for Cosmology, University of Cambridge, Madingley Road, Cambridge CB3 0HA, UK

<sup>4</sup> SISSA, Via Bonomea 265, 34136, Trieste, Italy

<sup>5</sup> INAF-Osservatorio Astronomico di Padova, Vicolo dell' Osservatorio 5, I-35122 Padova, Italy

<sup>6</sup> Spitzer Science Center, 314-6 Caltech, 1201 East California Boulevard, Pasadena, CA 91125, USA

<sup>7</sup> Department of Astronomy, 249-17 Caltech, 1201 East California Boulevard, Pasadena, CA 91125, USA

<sup>8</sup> National Radio Astronomy Observatory, P.O. Box 0, Socorro, NM 87801, USA

<sup>9</sup> INAF - Osservatorio Astronomico di Roma, via Frascati 33, 00040 Monteporzio, Italy

<sup>10</sup> INAF- Trieste Astronomical Observatory, via Tiepolo 11, 34143 Trieste, Italy

<sup>11</sup> Scuola Normale Superiore, Piazza dei Cavalieri 7, 56126, Pisa, Italy

<sup>12</sup> Physics Department, New Mexico Tech, Socorro, NM 87801, USA

<sup>13</sup> Department of Astronomy, Kyoto University, Kyoto 606-8502, Japan

<sup>14</sup> Dipartimento di Fisica e Astronomia, Università di Bologna, Viale Berti Pichat 6/2, I-30127, Bologna, Italy

<sup>15</sup> INAF-Osservatorio Astronomico di Bologna, Via Ranzani 1, I-40127 Bologna, Italy

<sup>16</sup> Square Kilometre Array Organization, Jodrell Bank Observatory, Lower Withington, Macclesfield, Cheshire SK11 9DL, UK

May 22, 2022

## ABSTRACT

The origin of the Cosmic Infrared Background (CIB) is still poorly understood, and represents a challenge from both the theoretical and observational points of view. We analysed 18 ALMA continuum maps in band 6 and 7, with rms down to  $7.8 \mu\text{Jy}$ , to estimate differential number counts down to  $60 \mu\text{Jy}$  and  $100 \mu\text{Jy}$  at  $\lambda = 1.3 \text{ mm}$  and  $\lambda = 1.1 \text{ mm}$ , respectively. We improved the source extraction method to detect sources down to  $S/N = 3.5$ . We detected 50 faint sources ( $< 1 \text{ mJy}$ ) down to  $60 \mu\text{Jy}$ . Determining the fraction of CIB resolved by the ALMA observations is hampered by the large uncertainties plaguing the CIB measurements (a factor of four in flux). However, our results provide a solid lower limit to CIB intensity. Moreover, the flattening of the integrated number counts at faint fluxes strongly suggest that we are close to resolving 100% of the CIB. Our data imply that galaxies with  $\text{SFR} < 40 M_{\odot}/\text{yr}$  certainly contribute less than 50% to the CIB, and probably a much lower fraction, while the bulk of the CIB must be produced by galaxies with  $\text{SFR} > 40 M_{\odot}/\text{yr}$ . The differential number counts are in nice agreement with recent semi-analytical models of galaxy formation down to our faint fluxes, therefore supporting the galaxy evolutionary scenarios and assumptions made in these models.

**Key words.** galaxies: evolution - galaxies: formation - galaxies: high-redshift

## 1. Introduction

The extragalactic background light (EBL) is a diffuse and isotropic radiation in the Universe, covering the range between ultraviolet (UV) and far infrared (FIR) wavelengths (Fixsen et al. 1998). After the CMB, the EBL represents the second-most energetic background. The IR/mm spectrum of the EBL was measured with the COsmic Background Explorer (COBE) satellite for the first time in the 1998. The EBL spectral energy distribution is composed of two peaks: the cosmic optical background (COB) and the cosmic infrared background (CIB). The former is caused by the radiation from stars, while the latter is due to UV/optical light absorbed by dust and re-radiated in the infrared wavelength range. Therefore, EBL contains information about star formation processes and galaxy evolution in the Universe. The study of this emission helps us understand the star formation evolution over the history of the Universe. In particular, we aim to understand the origin of the CIB, as it depends on the integrated history of energy production in the post-recombination Universe (Kashlinsky et al. 2005).

At  $850 \mu\text{m}$ , more than half of the CIB is emitted by submillimeter galaxies (Viero et al. 2013; Cai et al. 2013). The definition of submillimeter galaxies (SMGs) is somewhat loose and it is generally meant to indicate the bright end of the population of sources emitting at submm wavelengths, initially discovered by bolometers at single dish telescopes. SMGs are predominately high-redshift ( $z \geq 1$ ) star-forming galaxies with star formation rates (SFR) approaching  $1000 M_{\odot} \text{ yr}^{-1}$ , or even higher (e.g Blain et al. 2002). In these galaxies the bulk of the UV/optical emission from young stars is absorbed by the surrounding dust which, then, emits in the FIR wavelengths (Casey et al. 2014). Recent studies have shown that massive red-and-dead galaxies share the same clustering properties as SMGs. Thus, SMGs may be the progenitors of local massive elliptical galaxies (Simpson et al. 2014; Toft et al. 2014). Moreover, the high SFR typical of these sources suggests that bright SMGs ( $> 1 \text{ mJy}$ ) may contribute up to half of the co-moving SFR density at  $z \sim 2$  (Hughes et al. 1998; Blain et al. 1999; Smail et al. 2002; Wardlow et al. 2011; Casey et al. 2013).

However, SMGs represent an extreme class of objects, not representative of the bulk of the galaxy population at high- $z$  ( $z \gtrsim 1$ ). Most high- $z$  galaxies show a much lower SFR and are likely associated with systems evolving through secular processes (e.g. Rodighiero et al. 2011). For the bulk of the high- $z$  population, the rest-frame far-IR/submm properties (which provide information on obscured star formation and dust content), at mm/submm fluxes below 1 mJy, are still poorly known.

In the past decades the SCUBA and LABOCA surveys resolved 20% to 40% of the CIB at 850  $\mu\text{m}$  (e.g. Eales et al. 1999; Coppin et al. 2006; Weiß et al. 2009) and 10% to 20% of the CIB at 1 mm by deep surveys with the AzTEC camera (Wilson 2008). Until recently, the number counts of fainter sources ( $S < 1$  mJy) were not well constrained because of the limited sensitivity. However, single-dish surveys suggested that more than 50% of the CIB is emitted by faint sources with flux densities  $< 1$  mJy.

Recently, the number counts of faint mm sources, at fluxes fainter than 1 mJy, have been inferred thanks to high sensitivity and high resolution observations obtained with the Atacama Large Millimeter/submillimeter Array (ALMA). Hatsukade et al. (2013) claimed to have resolved  $\sim 80\%$  ( $\sim 13$  Jy  $\text{deg}^{-2}$ ) of the CIB at 1.3 mm exploring faint (0.1 - 1 mJy) sources with signal-to-noise  $\geq 4$  extracted from ALMA data. A similar result has been obtained at 1.2 mm by Ono et al. (2014), who suggest that the main contribution to the CIB comes from faint star-forming galaxies with  $\text{SFR} < 30 M_{\odot}/\text{yr}$ . However, as we shall discuss later on, the uncertainties on the CIB are extremely large and, once these are taken into account, the fraction of resolved background at these fluxes, as well as the identification of the sources contributing to the bulk of the CIB, are much more uncertain than given in these papers.

We have used imaging from ALMA with a sensitivity down to 7.8  $\mu\text{Jy}/\text{beam}$  (rms), which enabled us to achieve some of the faintest continuum detections at 1.1 mm and 1.3 mm with flux densities down to 60  $\mu\text{Jy}$ . The source counts presented here, thus, provide constraints on models of galaxy evolution and predictions for future ALMA follow-up surveys.

This paper is organised as follows. In Section 2, we describe the ALMA observations used in this work. Section 3 is focused on the source extraction technique. Section 4 presents the number counts we derived and the comparison between our results and recent galaxy formation models. In Section 5, we discuss and summarise our results.

## 2. Observations and data reduction

Our source extraction is applied to 18 continuum maps with high sensitivities, which were obtained in ALMA cycle 0 and cycle 1. For our analysis we focused on observations in band 6 and 7, since these are some of the deepest observations available. In this section we will describe in detail the ALMA Band 6 and 7 datasets used for the analysis.

The faintest sources are detected in three ALMA datasets taken by Maiolino et al. (in prep) who targeted three  $\text{Ly}\alpha$  emitters at  $z \sim 6-7$ : BDF-3299, BDF-521 and SDF-46975 (Vanzella et al. 2011; Ono et al. 2012). The BDF-3299 data (field *a* in Tab. 1) were observed during two different epochs: a first observation in October-November 2013 and a second one in April 2014. The target was observed with 27 12m antennae array in 2013 and 36 12m antennae array in 2014, with a maximum baseline of 1270 m. The flux densities were scaled with the observation data of J223-3137 and J2247-3657. The total on source integration time was  $\sim 5.2$  hrs. The other two sources, BDF-521 and SDF-46975,

were observed in November 2013 and March 2014, respectively (field *c* and *e* in Tab. 1). 29 12m antennae were used in the extended configuration of 17-1284 m baseline for BDF-521 and 40 12m antennae with maximum baseline of 422 m for SDF-46975. We used the observations of J223-3137 to scale the flux density. The total on source observing time was about 83 min and 121 min, respectively for the two targets.

We analysed 9 continuum maps (fields *j-r* in Tab. 1) taken by PI Capak, who targeted [CII] emission line from sources at high-redshift ( $z \geq 5$ ). The data were taken in November 2013 using 20 antennae in band 7. The total on source integration was about 20 min for each.

We also used ALMA data (field *b* in Tab. 1) for the  $\text{Ly}\alpha$  emitter at  $z = 7.215$ , SXDF-NB1006-2 (PI K. Ota; Shibuya et al. 2012). The target was observed on May 3-4 2014, with a maximum baseline of  $\sim 558$  m. The total on source observing time of the 37 12 m antennae was 106 min. The flux densities were scaled with the observation data of J0215-0222.

In addition to these maps, we analysed public archival ALMA data to increase the number of detections at intermediate flux densities. We selected only continuum maps in band 6 and 7 with sensitivity  $\leq 50 \mu\text{Jy}/\text{beam}$ , since we were interested in analysing the number count at flux densities  $< 1$  mJy that contribute to  $> 60\%$  of the CIB (Ono et al. 2014). Therefore, we analysed the data with the highest sensitivity taken by Willott et al. (2013) (fields *f* and *i* in Tab. 1), Ota et al. (2014) (fields *g* in Tab. 1), MacGregor et al. (2013) (fields *h* in Tab. 1) and Ouchi et al. (2013) (fields *d* in Tab. 1). Further details on the ALMA observations are summarised in those papers.

All ALMA data were reduced using the CASA v4.2.1 package. The typical flux uncertainties in the millimeter regime are  $\sim 10\%$ . The continuum maps were extracted using all the line-free channels of the four spectral windows. Unfortunately, in this version of CASA, the data weights are not set proportionally to the channel width and integration time, so they had to be adjusted whenever a continuum image was made from spectral windows that did not have the same channel width and index number. Furthermore, the data weights have to be fixed when a dataset is composed of different observations taken at different epochs, with different integration times and different observing (water vapour) conditions. In the case of BDF-3299, BDF-521 and SDF-46975, the data weights were manually re-scaled as a function of integration time and channel width. The continuum maps were cleaned using the CASA task “clean” with WEIGHTING= “natural”, achieving a sensitivity of about 7.8-52.1  $\mu\text{Jy}/\text{beam}$ . The correlator of each observations was configured to provide four independent spectral windows, so the central frequency  $\nu_{\text{obs}}$  in Table 1 is equivalent to the mean frequency of the four bands. The continuum map sensitivity and the area mapped in each observation are summarised in Table 1. The source extraction was performed out to two primary beams, after masking the targeted source of each observation, so as to not bias the final counts determination. Around all of these sources we placed 1'' diameter mask ( $\sim$  ALMA beam) since most of the main targets were non spatially resolved. In the particular case where the main target is extended (e.g. MacGregor et al. 2013) the dimension of the mask is as large as the size of the target, where the size of the target is estimated from its surface brightness emission down to  $3\sigma$ . In the worst case we masked about 5% of the field of view. The combined fields result in a total area of  $\sim 9.5 \times 10^{-4} \text{ deg}^2$  at 1.1 mm and  $\sim 6.6 \times 10^{-4} \text{ deg}^2$  at 1.3 mm

**Table 1.** ALMA Survey fields used in this paper, sorted by sensitivity.

Project code	$\nu_{\text{obs}}$ [GHz]	$\sigma$ [ $\mu\text{Jy beam}^{-1}$ ]	$\lambda$ [mm]	area [arcsec <sup>2</sup> ]	field
2012.A.00040.S	230	7.8	1.28	1520	a
2012.1.00374.S	225	14.5	1.31	1520	b
2012.1.00719.S	230	17.7	1.30	1520	c
2011.1.00115.S	232	18.6	1.29	1130	d
2012.1.00719.S	244	19.5	1.23	1390	e
2011.1.00243.S	250	20.9	1.2	1260	f
2011.1.00767.S	260	20.9	1.16	1520	g
2012.1.00142.S	230	26.3	1.28	1390	h
2011.1.00243.S	249	28.9	1.2	1260	i
2012.1.00523.S	286	29.9	1.05	920	j
2012.1.00523.S	295	30.0	1.02	920	k
2012.1.00523.S	286	30.3	1.05	920	l
2012.1.00523.S	289	33.1	1.05	920	m
2012.1.00523.S	290	36.3	1.03	920	n
2012.1.00523.S	289	38.1	1.05	920	o
2012.1.00523.S	289	41.8	1.05	920	p
2012.1.00523.S	292	49.1	1.02	920	q
2012.1.00523.S	292	52.1	1.02	920	r

Notes:  $\nu_{\text{obs}}$  is the mean frequency of the four spectral windows

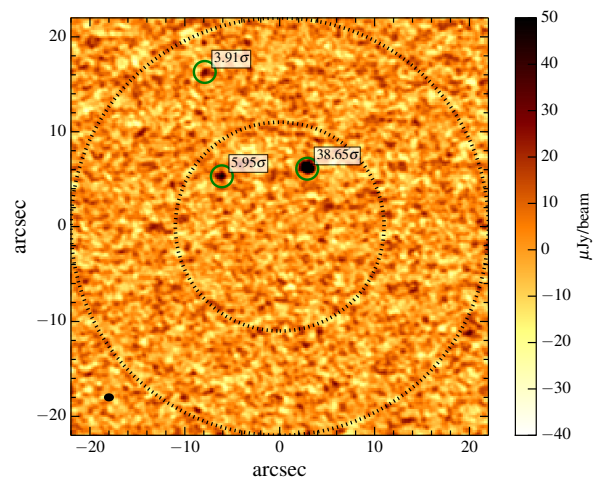
### 3. Source extraction

In total we analysed 18 ALMA continuum maps to derive the number counts of sources at millimetre wavelengths. Since we do not yet know either the spectral energy distributions (SEDs) or the redshifts of our faint mm sources, we estimated the number counts at two different wavelengths, 1.1 mm and 1.3 mm, to minimise the effects of wavelength extrapolation. The flux densities,  $S$ , of sources detected at wavelengths less than 1.2 mm were scaled to the 1.1 mm flux density and while counts at  $\lambda > 1.2$  mm were scaled to 1.3 mm using a modified blackbody with values typical of SMGs at  $z=2$ ; we adopted a spectral index  $\beta = 2.0$  and dust temperature  $T = 35$  K from Greve et al. (2012), who measured the spectral energy distribution from a sample of SMGs at the same wavelength range of our data. In the following we describe in detail the source extraction method and the statistical assessment.

#### 3.1. Source Catalogue

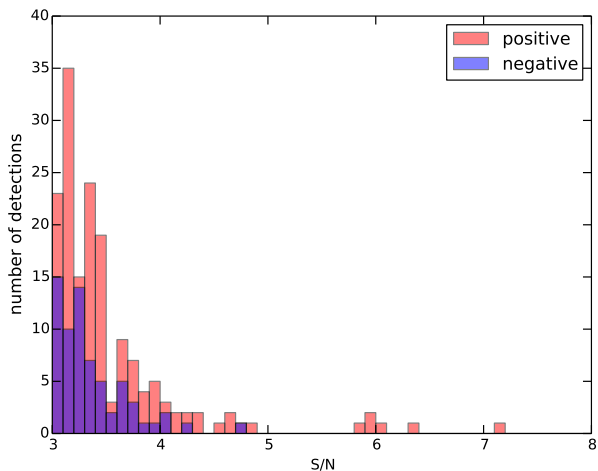
The source extraction was performed within an area as large as two primary beams, which has a diameter of about  $20''$ , before correcting for the primary beam attenuation. We first extract the sources fulfilling the following requirement: 1) the source should be above the  $3\sigma$  threshold in its continuum map (we will then take a more conservative threshold of  $3.5\sigma$ , as discussed later on); 2) the size of the 2D Gaussian fitting the putative source must be consistent, within the errors, with the beam size of the selected map (or at most marginally resolved, within 1.5 times the beam size). Indeed, most faint sources are not expected to be spatially resolved at the resolution of our maps. Detections with dimensions smaller than the beam must be associated with noise fluctuation of individual antennae or a group of antennae, or due to sidelobes of bright sources.

Figure 1 shows an example of an ALMA map in which the source extraction was performed down to  $3\sigma$  with the above requirements. At this low significance level ( $> 3\sigma$ ), some of these source candidates are likely to be spurious, due to noise fluctu-



**Fig. 1.** Example of a band 6 continuum map obtained with ALMA (field *a* Table 1). The green circles represent the sources detected with  $S/N > 3.5\sigma$  that also fulfil the requirement of having a size consistent with the beam (or marginally resolved). The inner black dotted circle indicates the primary beam and outer circle shows twice the primary beam. The synthesised beam is indicated by a filled black ellipse in the lower left corner of the plot.

ations. To define a more solid detection threshold, we estimated the number of spurious sources expected in the maps by applying the source extraction method to the continuum maps multiplied by  $-1$ , so as to estimate the number of negative sources as a function of the signal-to-noise ratio ( $S/N$ ). Figure 2 shows the number of positive and negative sources as a function of  $S/N$ . The number of the negative sources is almost always less than that of the positive at  $S/N > 3$ , suggesting that down to  $3\sigma$  some fraction of the positive detections are real (most of the negative sources and false positive sources are removed from the second requirement in the source extraction process). Since in previous works from Hatsukade et al. (2013) and Ono et al. (2014) the



**Fig. 2.** Number of positive (red) and negative (blue) sources, detected in the 18 continuum maps, as a function of signal-to-noise ratio (S/N).

number of positive sources was found to be larger than the number of negative ones at  $S/N > 3.5$ , we decided to be conservative and include in our catalogue only those objects satisfying the  $S/N > 3.5$  criterion.

In the 18 continuum maps we detected 50 sources with  $S/N$  in the range 3.5–38.4 and none of them appear to be marginally resolved.

### 3.2. Completeness and Survey Area

For each ALMA map  $i$ , we estimated the completeness,  $C_i(S)$ , that is the expected probability at which a real source with flux  $S$  can be detected, within the entire field of view considered by us (i.e. two primary beams).  $C_i(S)$  is calculated in each ALMA map corrected for primary beam attenuation. To estimate the completeness we inserted artificial sources with a given flux density  $S$  (at which we want to estimate the completeness). The positions of these artificial sources are randomly distributed within the 2-primary beams. The input source is considered to be recovered when it is extracted with  $S/N \geq 3.5\sigma$ . Within the selected flux densities range (0.05 to 1 mJy) we iterated the procedure of inserting artificial sources for each continuum maps 1000 times, using 4–8 artificial source in each simulation for each field. The completeness calculated in each map,  $C_i(S)$ , is equal to the ratio between the number of recovered sources and the number of input sources, for each flux  $S$ . Figure 3 shows  $C_i(S)$  as a function of the intrinsic flux density  $S$ , estimated on the deepest ALMA continuum map (field  $a$  in Table 1).

The beam response is not uniform and decreases on the distance from the map centre. Therefore the effective area sensitive to a given flux  $S$  decreases rapidly with the flux itself. As a consequence, the effective area of the survey depends on the considered flux, i.e.  $A_{\text{survey}}(S)$ . Since the completeness  $C_i(S)$  is estimated on the continuum maps corrected for primary beam attenuation, the completeness function already automatically includes the effect of variation of sensitivity as a function of distance from the map center. Therefore, the effective survey area of each map at a given flux  $S$  is given by  $C_i(S)A_i(S)$ , where  $A_i(S)$  is the 2-primary beam area of the ALMA map  $i$ . Therefore, the total effective survey area is given by

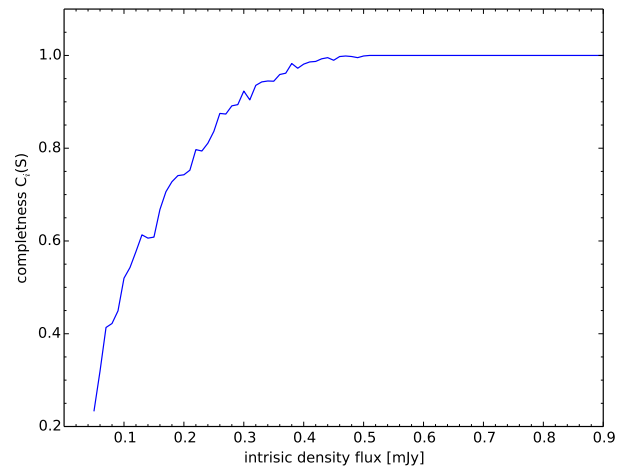


**Fig. 3.** Completeness  $C_i(S)$  as a function of the flux density  $S$  estimated from simulations. The solid curve is the result for field  $a$  with  $\text{rms} = 7.8 \mu\text{Jy}/\text{beam}$ .

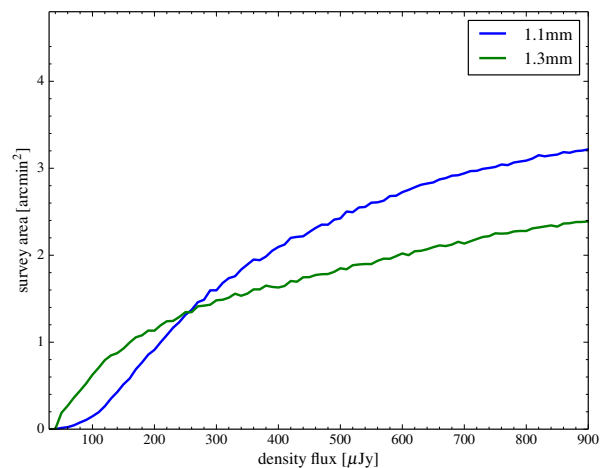


**Fig. 4.** Effective survey area as a function of intrinsic flux density. This is the area over which a source with an intrinsic flux density  $S$  can be detected with  $S/N > 3.5\sigma$ . The blue and green curves are the survey areas for the maps at 1.1 mm and 1.3 mm, respectively.

$$A_{\text{survey}}(S) = \sum_i C_i(S)A_i(S).$$

We obtained  $A_{\text{survey}}(S)$  both at 1.1 mm and at 1.3 mm, as shown in Figure 4.

### 3.3. Flux boosting

The noise fluctuations in continuum maps may influence photometric measurements of the extracted sources. Since the counts of faint sources increase with decreasing of flux density (e.g. Scott et al. 2012; Hatsukade et al. 2013; Ono et al. 2014), there should be a ‘sea’ of faint source below the noise level that may influence photometric extraction. There is, indeed, a greater probability that intrinsically faint sources are detected at higher flux than that bright ones are de-boosted to a lower flux. See Hogg & Turner (1998) for a full description of this effect. This

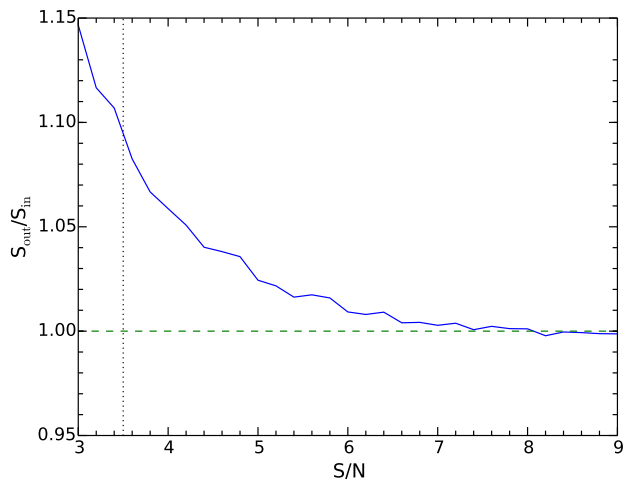


**Fig. 5.** Flux boosting factor as a function of S/N estimated from simulations. The horizontal dashed line corresponds to  $S_{\text{out}} = S_{\text{in}}$ . The vertical dashed line corresponds to the detection threshold,  $S/N = 3.5$ .

effect, called “flux boosting”, is extremely important at low S/N ( $< 5$ ) where flux measurement can be overestimated. Since we do not know the priori distribution of flux densities in the range 0.001-1 mJy, we performed a simple simulation to estimate the boost factor as a function of S/N detection.

The simulation was carried out in the map uncorrected for primary beam attenuation. We inserted into the maps flux-scaled artificial sources (4-8), whose S/N are in the range of 3-8. Then, we extracted the flux densities at the same position where the sources have been located. The flux boosting is calculated as the fraction of the measured flux density ( $S_{\text{out}}$ ) to the input flux density ( $S_{\text{in}}$ ). We repeated this simulation for each ALMA continuum map  $10^4$  times. Figure 5 shows the average ratio of the extracted flux densities  $S_{\text{out}}$  to the input flux densities  $S_{\text{in}}$  as a function of S/N. At  $S/N = 3.5$ , the boost fraction is  $\approx 1.09$ , so the difference between extracted flux and input flux is less than 10%. The boosting factor correction (Figure 5) was then applied to the measured detection fluxes.

## 4. Results

### 4.1. Differential number counts

Summarising the previous sections: we detected 50 sources with  $S/N > 3.5$  in 18 continuum maps in ALMA band 6 and 7, with the additional (more conservative) requirements given in section 3.1. Then, we corrected the flux densities for the “flux boosting” effect. We scaled the flux density of the sources observed at  $\lambda < 1.2$  mm to the flux density at 1.1 mm and those at  $\lambda > 1.2$  mm to the flux density at 1.3 mm. Following the prescription of Hatsukade et al. (2013) and Ono et al. (2014) we estimated the number counts at two different wavelengths: 1.1 mm and 1.3 mm. We then estimated the effective survey area associated with the flux of each source. To estimate the number counts, we corrected for the contamination of “spurious” sources, i.e. the fraction of sources due to noise fluctuations above the  $3.5\sigma$  level (and meeting the additional requirements given in sect 3.1). The contamination fraction  $f_c$  was inferred from the fraction of negative sources at each S/N level, as inferred from Figure 2. For each source  $f_c$  is the ratio between negative and positive detections at its S/N. Therefore, the contribution of each source to the

**Table 2.** Differential number counts.

$\lambda = 1.1$ mm		
S [mJy]	$dN/d\text{Log}(S)$ [ $10^4$ ]	$N_{\text{source}}$
0.13	$10^{+7}_{-4}$	5
0.20	$11^{+3}_{-3}$	14
0.30	$2^{+2}_{-1}$	3
0.63	$0.7^{+0.9}_{-0.4}$	2
$\lambda = 1.3$ mm		
S [mJy]	$dN/d\text{Log}(S)$ [ $10^4$ ]	$N_{\text{source}}$
0.06	$11^{+14}_{-7}$	2
0.08	$10^{+7}_{-4}$	5
0.12	$7^{+4}_{-3}$	7
0.22	$3^{+2}_{-2}$	5
0.34	$4^{+2}_{-2}$	7

number counts is  $(1-f_c)$  divided by its respective effective survey area  $A_{\text{survey}}(S)$ . We carried out the logarithmic differential number counts  $dN(S)/d\text{Log}S$  in logarithmic flux density bins with size  $\Delta\text{Log}S = 0.2$ . So the logarithmic differential number counts for a selected bin is given by:

$$\left. \frac{dN(S)}{d\text{Log}S} \right|_{S \pm 1/2\Delta\text{Log}S} = \sum_j \frac{1 - f_{c,j}}{A_{\text{survey}}(S)}$$

where  $j$  are all sources with flux density between  $\text{Log}S - 1/2\Delta\text{Log}S$  and  $\text{Log}S + 1/2\Delta\text{Log}S$ . The resulting differential number counts are scaled to  $\Delta\text{Log}S = 1$ .

The uncertainty on the logarithmic differential number counts are calculated from Poisson confidence limits of 84.13% (Gehrels 1986) by using the number of sources detected in each bin. The resulting differential number counts are summarised in Table 2 and shown in Figure 6 (blue solid symbols). Number counts could be derived down to  $60\mu\text{Jy}$  at 1.3mm and down to  $100\mu\text{Jy}$  at 1.1mm. We also show separately (hollow symbols) the number counts inferred by only using the sources detected within the primary beam (i.e. 7 sources at 1.1 mm and 6 sources at 1.3 mm). In the latter case the statistical errorbars are obviously larger, but fully consistent (within errors) with the number counts inferred over two beams.

We also show the number counts of bright ( $S > 1$  mJy) SMGs obtained by Scott et al. (2012) at 1.1 mm with AzTEC. However, the two faintest bins in the latter data will not be considered when comparing models or to fit analytic functions, since the completeness at these flux densities is too low and the number counts are underestimated. Since there are no number counts of bright sources at 1.3 mm, we used the number counts at 1.1 mm by scaling the flux density to 1.3 mm flux density. Figure 6 shows that the differential number counts increase with decreasing flux density. At 1.3 mm, the differential number counts of Hatsukade et al. (2013) (orange symbols), which are obtained from sources with  $S/N \geq 4$ , are consistent with our results within the uncertainties, but our slope of the logarithmic number counts at sub-mJy flux densities is flatter than those obtained by Hatsukade et al. (2013). We do not plot the number counts of Ono et al. (2014) as they were estimated at 1.2 mm using continuum maps over the whole 1.04-1.22 mm wavelength range, i.e. they were not extracted with the same procedure we used to define our sample. Given that there is no information yet on the SED or

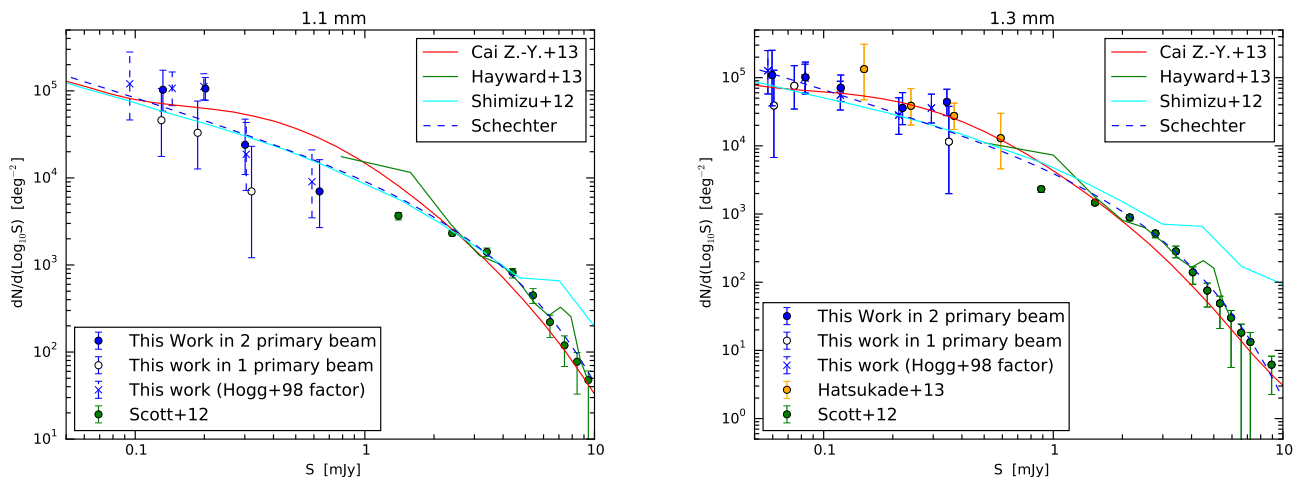


**Fig. 6.** Logarithmic differential number counts as a function of flux density at  $\lambda = 1.1$  mm and  $\lambda = 1.3$  mm. The blue solid symbols are the results of this work. The hollow symbols are the results obtained by using only the sources within one primary beam. The blue crosses with dashed error-bars are the differential number counts corrected for “flux boosting” by using equation 4 in Hogg & Turner (1998). The green symbols are estimated from Scott et al. (2012). The orange symbols are the number counts estimated by Hatsukade et al. (2013). The red, cyan and green solid curves are the model predictions of obtained by Cai et al. (2013), Shimizu et al. (2012), and Hayward et al. (2013), respectively. The blue dashed curve shows the best-fit Schechter function.

on the redshift of the sources contributing to the number counts, we believe that our approach of dividing sources in to two wavelength ranges, hence minimising the extrapolation assumptions, provide more solid results.

We also show (with crosses and dashed error-bars) the differential number counts by correcting for a boost factor estimated from equation (4) of Hogg & Turner (1998) (note that the correction was on the data *not* corrected for flux boosting as described in Sect. 3.3, else this would result in a double correction). In order to apply the prescription of Hogg & Turner (1998) we used the best-fit Schechter function (Sect. 4.3) as a conservative a priori distribution of flux densities at faint fluxes (we shall see that a Schechter function tend to give an extrapolation of the number counts that is steeper than expected by models and tend to overproduce the CIB). It should however be noted that the prescription given by Hogg & Turner (1998) may not apply to these data, since the noise is not uniformly distributed over the field of view as a consequence of the primary beam attenuation. Anyway, as seen in Figure 6, the slopes obtained with this correction factor is consistent with ones obtained using a boost factor estimated in Sec. 3.3.

#### 4.2. Comparison with models

We compared the differential and integrated number counts to the theoretical results obtained by recent simulations and semi-analytical models. In Figure 6, the differential number counts by Hayward et al. (2013) are shown with a green line. Their results were obtained by combining a semi-analytical model with 3-D hydrodynamical simulations and 3-D dust radiative transfer calculations. The main contributions to the mm counts is from isolated-disc, galaxy pairs, and late-stage merger induced starbursts. Figure 6 shows that their model predictions are able to reproduce the observational results at flux densities  $> 2$  mJy,

We also compared our results with the model by Shimizu et al. (2012), who performed cosmological hydrodynamics simulations using an updated version of the Tree-PM smoothed particle hydrodynamics code GADGET-3. They assumed feedback

mechanisms to be triggered by supernovae and the SED of galaxies at mm-FIR wavelengths to be described by a modified black body emission. This model predicts that the bright SMGs reside in greater massive halos ( $> 10^{12} M_{\odot}$ ) and that their typical stellar masses are greater than  $10^{11} M_{\odot}$ . Their results are broadly consistent with the ALMA results up to 1–5 mJy. However, their estimated number counts of bright SMGs ( $> 1 - 5$  mJy) are significantly higher than the observed number counts both at 1.1 and 1.3 mm. According to this model, approximately 90% of millimetre sources in the flux range of 0.1-1 mJy are at  $z > 2$ . Therefore most of the observed sources are high- $z$  galaxies, and the contribution from low- $z$  is small.

Finally, Figure 6 shows the theoretical predictions of Cai et al. (2013)<sup>1</sup>. The Cai et al. (2013) model starts from considering the observed dichotomy in the ages of stellar populations of massive spheroidal (components of) galaxies on one side and late-type galaxies on the other. Spheroidal galaxies and massive bulges of Sa’s must have formed most of their stars at  $z \gtrsim 1$ , while the disc components of spirals and the irregular galaxies are characterised by significantly younger stellar populations and star formation activity continuing up to the present time. The evolution of spheroidal components is described by a physical model relying on published results of high resolution  $N$ -body simulations showing that pre-galactic halos undergo an early phase of fast collapse, including a few major merger events, during which the central regions rapidly reach a dynamical quasi-equilibrium. This phase is followed by a slow growth of the halo outskirts in the form of many minor mergers and diffuse accretion, that has little effect on the inner potential well where the visible galaxy resides. The evolution of the visible galaxy is, then, generally (although not always) driven by internal baryonic processes, ruled by a set of equations, laid down in the Appendix of Cai et al. (2013). These equations take into account the energy feedback from supernovae and the active nucleus. The model includes a self consistent treatment of the chemical evolution of the ISM, calculated using the standard equations

<sup>1</sup> The models predictions are available in electronic format at the Web site <http://staff.ustc.edu.cn/~zcaif/>

and stellar nucleosynthesis prescriptions. The chemical evolution controls the evolution of the dust abundance, hence the dust absorption and re-emission. On the other hand, the evolution of Late-type galaxies was described using a phenomenological approach, considering two populations with different spectral energy distributions (SEDs) and different evolutionary properties: “normal” late-type galaxies, with low evolution and low dust temperatures (“cold” population) and rapidly evolving starburst galaxies, with warmer dust temperatures (“warm” population). Their results are in good agreement with our differential number counts from faint to bright density fluxes at 1.3 mm and also 1.1 mm (although with some deviations). According to this model the steep slope of the bright counts is accounted for by the sudden appearance, at  $z \gtrsim 1.5$  of star-forming proto-spheroidal galaxies whose counts begin to flatten already at flux densities of a few to several mJy’s. The counts of starburst galaxies have a somewhat flatter slope and come up at levels similar to those of proto-spheroids at the flux densities of the (new) faint counts, while the contribution of “normal” late-type galaxies is always minor in the considered flux density range but increases with decreasing flux density. The redshift distribution at the flux densities of the present counts is bimodal, with starburst galaxies peaking at  $z \approx 1.5$  and proto-spheroids peaking at  $z \approx 2$ . At bright flux densities ( $S \sim 10$  mJy) the starburst galaxy peak shifts to  $z \ll 1$  (since the brightest, in flux terms, starburst galaxies are mostly local) while the proto-spheroid one remains at  $z \approx 2$ .

#### 4.3. Source counts parametrization with a Schechter function

We also parametrised the differential number counts using a Schechter function:

$$\frac{dN}{dS} dS = \phi_{\star} \left( \frac{S}{S_{\star}} \right)^{\alpha} \exp\left(-\frac{S}{S_{\star}}\right) d\left(\frac{S}{S_{\star}}\right)$$

with  $\phi_{\star}$  being the normalisation,  $S_{\star}$  the characteristic flux density, and  $\alpha$  the faint-end slope of the number counts. We fitted separately the Schechter function at 1.1 mm and 1.3 mm by using the number counts estimated in this work and from the literature (e.g. Scott et al. 2012, Hatsukade et al. 2013). We did not use the two faintest data points from Scott et al. (2012) because they may suffer from completeness problems. The three free parameters were then derived by  $\chi^2$  minimisation. Table 3 reports the best-fit parameters and Figure 6 and 7 show the results of the Schechter function fitting.

The reduced  $\chi^2$  are 0.9 and 1.1 at 1.1 mm and 1.3 mm, respectively, meaning that the differential number counts can be properly described by a Schechter function down to the flux levels observed by us. The two faint-end slopes are similar within the errors, suggesting that the two number counts can be described by the same function. The bright-end shape also matches perfectly well a pure Schechter function at both wavelengths, which has recently been observed in Dayal et al. (2014).

However, we note that the slope of the Schechter function is significantly steeper than expected by models (especially at 1.3 mm) and would overproduce the CIB at faint fluxes, even by taking the upper boundary of the CIB, which will be discussed in the next section. Therefore, we warn that the Schechter function fitted to the current data is probably not suitable for describing the number counts at fluxes fainter than observed by us.

**Table 3.** Best fit parameters of the Schechter function at  $\lambda = 1.1$ , and  $\lambda = 1.3$  mm.

$\lambda$	$\phi_{\star}$ [deg $^{-2}$ ]	$S_{\star}$ [mJy]	$\alpha$
1.1 mm	$(2.7 \pm 0.9) \times 10^3$	$2.6 \pm 0.4$	$-1.81 \pm 0.14$
1.3 mm	$(1.8 \pm 0.4) \times 10^3$	$1.7 \pm 0.2$	$-2.08 \pm 0.11$

#### 4.4. Cosmic infrared background

We calculated the 1.1 mm and 1.3 mm number counts down to  $60 \mu\text{Jy}$  using Cycle 0 and 1 ALMA observations. Using the improved number counts estimated in this work, we estimated the integrated flux densities from resolved sources and we derived the fraction of the CIB resolved by ALMA at 1.1 mm and 1.3 mm. The integrated flux densities are given by

$$I(S > S_{\text{lim}}) = \int_{S_{\text{limit}}}^{\infty} \frac{dN(S)}{dS} S dS$$

where

$$\frac{dN(S)}{dS} = \frac{dN(S)}{d\text{Log}S} \frac{1}{S \ln(10)}$$

Figure 7 shows the integrated flux densities at 1.1 mm and 1.3 mm as a function of  $S_{\text{limit}}$ . Note that we used the results of Scott et al. (2012) at bright flux ( $S > 1$  mJy), but excluding the two point at faintest fluxes, because of incompleteness issues. The integrated counts down to  $S_{\text{limit}} = 0.1$  mJy at 1.1 mm and to  $S_{\text{limit}} = 0.06$  mJy at 1.3 mm are  $17^{+10}_{-5}$  Jy deg $^{-2}$  and  $13^{+6}_{-3}$  Jy deg $^{-2}$  respectively. We compared these results with the analytical fit obtained by Fixsen et al. (1998) from the COBE measurement:  $25^{+22}_{-13}$  Jy deg $^{-2}$  at 1.1 mm and  $17^{+16}_{-9}$  Jy deg $^{-2}$  at 1.3 mm (see also Lagache et al. 1999 and Schmidt et al. 2015). Since these measurements suffer from large uncertainties (especially due to the uncertainties on the Galactic contribution), we are not able to determine exactly the fraction of CIB resolved. Certainly, even by taking the highest value of the CIB consistent with the uncertainties given by Fixsen et al. (1998) we can say that at  $60 \mu\text{Jy}$  at least more than 50% (probably much more) of the CIB is resolved. Anyway our results provide a solid lower limit to the CIB intensity at 1.1 mm and 1.3 mm. Moreover, the flatness of the faint end-slopes, in particular that at 1.3 mm, suggests that the integrated flux densities estimated in this work are likely close to the CIB intensity: within the errorbars our data are consistent with resolving nearly 100% of the CIB.

The blue curve gives the integrated number counts inferred from the Schechter function fitting the differential number counts, and the shaded blue area gives the associated uncertainty. The uncertainty of the latter is large enough to be consistent with any value of the CIB within the range given by Fixsen et al. (1998), however the slope would indicate that this functional form would saturate even the highest boundary at the CIB at faint fluxes, as discussed above.

It will be of great interest to investigate, with followup observations, what is the redshift distribution of these sources which produce most of the background, especially to the faint end. In the meantime we can infer what the properties are of these galaxies in terms of SFR. Indeed, because of the negative K-correction, at 1.3 mm a given observed flux density corresponds to an IR-luminosity (hence a SFR) nearly independent of redshift, across the entire redshift range  $0.5 < z < 15$  (by adopting the conversion factor and IMF given in Blain et al. 1999; Maiolino et al. 2008). In particular, the minimum flux density

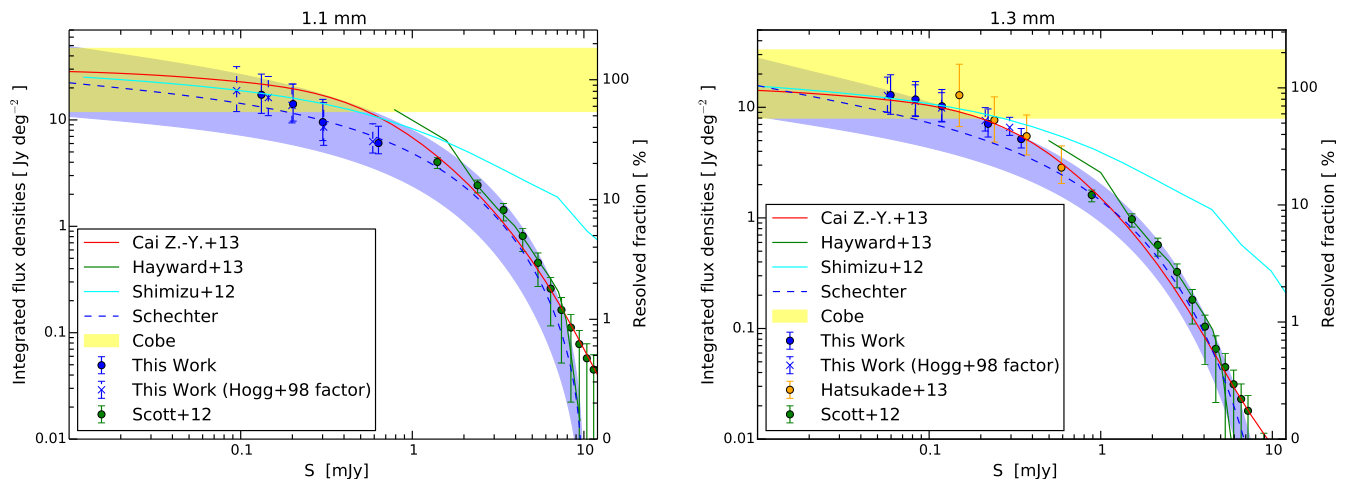


**Fig. 7.** Integrated flux density at  $\lambda = 1.1$  mm and  $\lambda = 1.3$  mm. The right axis shows the fraction of resolved CIB. The yellow shaded region is the CIB measured by COBE (Puget et al. 1996; Fixsen et al. 1998). The blue symbols are the results from this work (we used the differential number counts by Scott et al. (2012), green symbols, for  $S > 1$  mJy). The blue crosses with dashed error-bars are the results from this work corrected for the “flux boosting” by using equation 4 in Hogg & Turner (1998). The orange symbols are from the number counts estimated by Hatsukade et al. (2013). The red, cyan and green solid curve are the model prediction of obtained by Cai et al. (2013), Shimizu et al. (2012), and Hayward et al. (2013), respectively. The blue dashed curve shows the integrated flux densities estimated from the best-fit Schechter function and the blue shaded region indicates its statistical uncertainty.

sampled by us,  $60 \mu\text{Jy}$  at 1.3mm, corresponds to a total IR luminosity  $L(8 - 1000\mu\text{m}) = 6 \times 10^{44} \text{ erg s}^{-1}$ , corresponding to a  $\text{SFR} = 40 M_{\odot} \text{ yr}^{-1}$  (Kennicutt & Evans 2012), nearly independent of redshift. We can therefore state that galaxies with  $\text{SFR} < 40 M_{\odot} \text{ yr}^{-1}$  certainly contribute to less than 50% of the CIB at 1.3 mm, and probably a much lower fraction (if one takes into account that the flattening of the number counts, consistent with models, suggest that at our faint fluxes we are resolving most of the CIB). Viceversa, the bulk of the CIB (50% and probably much more) must be contributed by galaxies with  $\text{SFR} > 40 M_{\odot} \text{ yr}^{-1}$ .

## 5. Summary and conclusions

We have used 18 deep ALMA maps in band 6 and 7 to investigate the number counts of sources at millimeter wavelengths. The sensitivity (rms) of these ALMA maps range from  $7.8 \mu\text{Jy}/\text{beam}$  to  $52 \mu\text{Jy}/\text{beam}$ .

Sources were detected down to  $3.5\sigma$ . We applied, as requirement for detection, that the size of the sources should be equal to the beam size (or slightly larger) within the uncertainties. Since the noise due to bad uv-visibilitys, or to sidelobes emissions from bright sources, or thermal noise associated with individual antennae or group of antennae, should introduce fluctuations that have a spatial shape completely different from the coherent beam, this criterion enables us to remove most of the spurious detections associated with noise fluctuations.

We searched for sources out to a distance equal to diameter of two primary beams. However, we have checked that the final number counts do not change, within errors, by restricting the source search to within the primary beam (although the statistics is obviously lower).

A total of 50 sources were detected matching these criteria. We explored the number counts at two different wavelengths, 1.1mm and 1.3mm (hence the ALMA maps were divided into two groups depending on their central wavelength). This approach avoids large flux extrapolation from observations obtained at different wavelengths. Since we do not know yet the

intrinsic SED and redshift distribution of the detected sources (which would be required for a proper extrapolation of the fluxes from different wavelengths), our approach provides safer results, although at the expense of statistics.

Number counts were obtained by taking into account completeness, flux boosting effects, correction for spurious sources and effective survey area at different flux limits. We extracted differential number counts down to  $60 \mu\text{Jy}$  and  $100 \mu\text{Jy}$  at 1.3mm and 1.1mm, respectively, inferring sources number densities of  $dN/d(\text{Log}S) \sim 10^5 \text{ deg}^{-2}$  at these faint limits.

The differential number counts at 1.1mm (1.3mm), across the entire range from  $60 \mu\text{Jy}$  to 10 mJy, can be fitted with a Schechter function with a faint end slope  $\alpha \approx -1.8$  ( $\alpha \approx -2.0$ ), a characteristic flux density  $S_* \approx 2.6$  mJy ( $S_* \approx 1.7$  mJy) and a normalisation at  $S_*$  of  $\phi_* = 2.7 \times 10^3 \text{ deg}^{-2}$  ( $\phi_* = 1.8 \times 10^3 \text{ deg}^{-2}$ ). We note that such Schechter functions describe the number counts down to  $60\text{--}100 \mu\text{Jy}$ , but their extrapolation to fainter fluxes is not trustworthy.

The large uncertainties plaguing our knowledge of the CIB level prevent us to set tight limits on the fraction that is resolved by our data. Clearly, at least 50% of the CIB is resolved by our data (and probably much more). However, our results set a solid lower limit to the CIB intensity at 1.1-1.3 mm, significantly above the value coming from direct measurements. The flatness of the faint counts implies that this lower limit is likely close to the CIB intensity.

The SFR of the sources contributing to the CIB at such faint fluxes is about  $40 M_{\odot} \text{ yr}^{-1}$ , independent of their redshift. We therefore infer that sources with  $\text{SFR} < 40 M_{\odot} \text{ yr}^{-1}$  contribute to less than half of the CIB at 1.3 mm, and probably much less. Viceversa, the bulk of the CIB must be produced by galaxies with  $\text{SFR} > 40 M_{\odot} \text{ yr}^{-1}$ .

*Acknowledgements.* We thank Paola Adreani, Matthew Auger and Valentina Calvi for comments and discussions. This paper makes use of the following ALMA data: ADS/JAO.ALMA#2011.1.00115.S, ADS/JAO.ALMA#2011.1.00243.S, ADS/JAO.ALMA#2011.1.00767.S, ADS/JAO.ALMA#2012.1.00142.S, ADS/JAO.ALMA#2012.1.00374.S, ADS/JAO.ALMA#2012.1.00523.S, ADS/JAO.ALMA#2012.1.00719.S and

ADS/JAO.ALMA#2012.A.00040.S. ALMA is a partnership of ESO (representing its member states), NSF (USA) and NINS (Japan), together with NRC (Canada) and NSC and ASIAA (Taiwan), in cooperation with the Republic of Chile. The Joint ALMA Observatory is operated by ESO, AUI/NRAO and NAOJ.

## References

- Blain, A. W., Moller, O., & Maller, A. H. 1999, *MNRAS*, 303, 423
- Blain, A. W., Smail, I., Ivison, R. J., Kneib, J.-P., & Frayer, D. T. 2002, *Phys. Rep.*, 369, 111
- Cai, Z.-Y., Lapi, A., Xia, J.-Q., et al. 2013, *ApJ*, 768, 21
- Casey, C. M., Chen, C.-C., Cowie, L. L., et al. 2013, *MNRAS*, 436, 1919
- Casey, C. M., Narayanan, D., & Cooray, A. 2014, *Phys. Rep.*, 541, 45
- Coppin, K., Chapin, E. L., Mortier, A. M. J., et al. 2006, *MNRAS*, 372, 1621
- Dayal, P., Ferrara, A., Dunlop, J. S., & Pacucci, F. 2014, *MNRAS*, 445, 2545
- Eales, S., Lilly, S., Gear, W., et al. 1999, *ApJ*, 515, 518
- Fixsen, D. J., Dwek, E., Mather, J. C., Bennett, C. L., & Shafer, R. A. 1998, *ApJ*, 508, 123
- Gehrels, N. 1986, *ApJ*, 303, 336
- Greve, T. R., Vieira, J. D., Weiß, A., et al. 2012, *ApJ*, 756, 101
- Hatsukade, B., Ohta, K., Seko, A., Yabe, K., & Akiyama, M. 2013, *ApJ*, 769, L27
- Hayward, C. C., Narayanan, D., Kereš, D., et al. 2013, *MNRAS*, 428, 2529
- Hogg, D. W. & Turner, E. L. 1998, *PASP*, 110, 727
- Hughes, D. H., Serjeant, S., Dunlop, J., et al. 1998, *Nature*, 394, 241
- Kashlinsky, A., Arendt, R. G., Mather, J., & Moseley, S. H. 2005, *Nature*, 438, 45
- Kennicutt, R. C. & Evans, N. J. 2012, *ARA&A*, 50, 531
- Lagache, G., Abergel, A., Boulanger, F., Désert, F. X., & Puget, J.-L. 1999, *A&A*, 344, 322
- MacGregor, M. A., Wilner, D. J., Rosenfeld, K. A., et al. 2013, *ApJ*, 762, L21
- Maiolino, R., Nagao, T., Grazian, A., et al. 2008, *A&A*, 488, 463
- Ono, Y., Ouchi, M., Kurono, Y., & Momose, R. 2014, *ApJ*, 795, 5
- Ono, Y., Ouchi, M., Mobasher, B., et al. 2012, *ApJ*, 744, 83
- Ota, K., Walter, F., Ohta, K., et al. 2014, *ApJ*, 792, 34
- Ouchi, M., Ellis, R., Ono, Y., et al. 2013, *ApJ*, 778, 102
- Puget, J.-L., Abergel, A., Bernard, J.-P., et al. 1996, *A&A*, 308, L5
- Rodighiero, G., Daddi, E., Baronchelli, I., et al. 2011, *ApJ*, 739, L40
- Schmidt, S. J., Ménard, B., Scranton, R., et al. 2015, *MNRAS*, 446, 2696
- Scott, K. S., Wilson, G. W., Aretxaga, I., et al. 2012, *MNRAS*, 423, 575
- Shibuya, T., Kashikawa, N., Ota, K., et al. 2012, *ApJ*, 752, 114
- Shimizu, I., Yoshida, N., & Okamoto, T. 2012, *MNRAS*, 427, 2866
- Simpson, J. M., Swinbank, A. M., Smail, I., et al. 2014, *ApJ*, 788, 125
- Smail, I., Ivison, R. J., Blain, A. W., & Kneib, J.-P. 2002, *MNRAS*, 331, 495
- Toft, S., Smolčić, V., Magnelli, B., et al. 2014, *ApJ*, 782, 68
- Vanzella, E., Pentericci, L., Fontana, A., et al. 2011, *ApJ*, 730, L35
- Viero, M. P., Moncelsi, L., Quadri, R. F., et al. 2013, *ApJ*, 779, 32
- Wardlow, J. L., Smail, I., Coppin, K. E. K., et al. 2011, *MNRAS*, 415, 1479
- Weiß, A., Kovács, A., Coppin, K., et al. 2009, *ApJ*, 707, 1201
- Willott, C. J., Omont, A., & Bergeron, J. 2013, *ApJ*, 770, 13